



# Using poro-elasticity to model the large deformation of tissue during subcutaneous injection

Yu Leng<sup>\*</sup>, Mario de Lucio, Hector Gomez

*School of Mechanical Engineering, Purdue University, West Lafayette, IN 47907, United States*

Received 11 December 2020; received in revised form 25 March 2021; accepted 7 May 2021

Available online 2 June 2021

## Abstract

Subcutaneous injection of therapeutic monoclonal antibodies (mAbs) has recently attracted unprecedented interests in the pharmaceutical industry. The drug transport in the tissue and mechanical response of the tissue after injection are not yet well-understood. We are motivated to study subcutaneous injection using poro-elasticity, including linear and nonlinear poro-elastic models. We first present the fixed-stress split of the nonlinear model and perform convergence studies under spatial and temporal refinements. We then investigate the model assumption of the linear model using numerical solutions. In the case of small permeability, the linear model is not adequate to account for the large deformation of the tissue due to injection. Next, we adopt a nonlinear poro-elastic model to study subcutaneous injection. For large deformation, numerical solutions of the nonlinear model differ significantly from that of the linear model, especially near the injection site.

© 2021 Elsevier B.V. All rights reserved.

*Keywords:* Subcutaneous injection; Nonlinear poro-elasticity; Fixed-stress split; Large deformation; Finite element method

## 1. Introduction

In this work, we are motivated by the numerical study of subcutaneous administration of monoclonal antibodies (mAbs). Therapeutic mAbs are protein-based drugs which have shown great potential in the pharmaceutical industry [1]. Subcutaneous injection of mAbs attracts increasing attention from the patients and caregivers because it enables self-administration which reduces the cost of treatment including medical equipments and personnel expenses [2,3]. However, compared to intravenous administration, subcutaneous delivery suffers from low bioavailability [4], which is the amount of drug entering the systemic circulation, and limited drug volume [3,5]. It is of both economic and scientific interests to study the drug distribution in the subcutaneous tissue after administration and to optimize delivery strategies. The pressure gradient in the tissue is the main driving force of the drug transport, and the pressure at the injection site serves as an indicator for possible fracture initiations [6,7]. We start by investigating the mechanical response and the pressure of the tissue after drug delivery using poro-elasticity, which is the main focus of this work.

Poro-elasticity has been widely used to model hydrated biological tissues [8,9], such as brain [10–13], subcutaneous tissue [14], and cartilage [15,16]. Biphasic poro-elastic models [17,18] assume the tissue is composed

<sup>\*</sup> Corresponding author.

*E-mail address:* [leng10@purdue.edu](mailto:leng10@purdue.edu) (Y. Leng).

of two phases, solid and fluid. Under loading conditions, such as compression, tension, shear, and injection, the fluid phase is free to move in the tissue; at the same time the tissue deforms. If the deformation is small, poro-elastic models reduce to the linear model, which coincides with the Biot's consolidation theory [19–21]. The linear model was applied to subcutaneous injection in [14]. However, experiments show that the constitutive laws of adipose tissue are highly nonlinear [22–26]. The Ogden hyperelastic [23,26] and nonlinear viscoelastic models [22,24,25,27] have been used to characterize the adipose tissue behavior. Even though, the viscosity of the solid is important to cyclical compression, shear and tension tests [10,27], it remains to show if the solid viscosity is critical to subcutaneous injection [6]. In view of these studies, we adopt the Ogden hyperelastic constitutive relation in the framework of poro-elasticity to study the subcutaneous injection of mAbs.

We first present the fixed-stress iterative split [28–31], developed for linear poro-elasticity, to nonlinear poro-elastic models by splitting the strain–energy function of the solid into isochoric and volumetric contributions as shown in [17]. Convergence analysis is performed under spatial and temporal refinements. Fixed-stress split facilitates the use of different solvers, preconditioners and even numerical methods for the conservation of mass and momentum equations. Previously, monolithic solvers [10,32–34] and a splitting  $L$ -scheme [34] have been used to solve nonlinear poro-elastic models. To our best knowledge, this is the first time that the fixed-stress split is applied to nonlinear poro-elastic models.

Then, we validate the linear poro-elastic model, which was used to study subcutaneous injection in [14] without validation, using numerical simulations. Next, we use a nonlinear kinematic model (also adopted in [10,35–37]) combined with the Ogden hyperelastic constitutive relation, and compare the numerical solutions of the linear and nonlinear models using model parameters taken from experiments in [26].

This paper is organized as follows. In Section 2, we introduce the linear and nonlinear poro-elastic models following the Theory of Porous Media [17,38]. Section 3 discusses the numerical methods used in this work. Section 4 presents the fixed-stress split of the nonlinear poro-elastic model and its convergence studies. The linear and nonlinear poro-elastic models are then applied to study subcutaneous injection in Section 5. Finally, Section 6 summarizes the findings of this work.

## 2. Model equations

We assume the injected fluid, which contains a nonreactive drug (mAbs), shares the same physical properties, i.e., density and viscosity, as the interstitial fluid. The subcutaneous tissue is modeled as a biphasic material. In this section, we follow the notation of [10,17,38] and introduce the linear and nonlinear poro-elastic models used in this work.

### 2.1. Preliminary

We first introduce some concepts and notations that are used throughout the rest of the paper. Let  $\Omega_t \subset \mathbb{R}^d$ , where  $d = 3$  is the spatial dimension, be an open, bounded, and continuously deforming domain with Lipschitz boundary  $\partial\Omega_t$ , for all time  $t \in (0, T]$ , where  $T > 0$ .  $\Omega_t$  is referred to as the current or deformed configuration. At  $t = 0$ ,  $\Omega_0$  is the undeformed or initial configuration. A spatial point  $\mathbf{x} \in \Omega_t$  is also expressed as  $\mathbf{x} = (x, y, z)$ . Based on the Theory of Porous Media [10,17,37,39], the spatial point  $\mathbf{x} \in \Omega_t$  is occupied by two phases, fluid ( $f$ ) and solid ( $s$ ), simultaneously, i.e.,  $\mathbf{x} = \mathbf{x}_\alpha$ , for  $\alpha = s, f$ . We assume the tissue is fully saturated, such that

$$\sum_{\alpha=s,f} \phi_\alpha(\mathbf{x}, t) = 1, \text{ in } \Omega_t, \quad (1)$$

where  $\phi_\alpha(\mathbf{x}, t)$  is the volume fraction, defined as the volume of phase  $\alpha$  over the total volume at  $\mathbf{x}$  in the current configuration. We define two bijective mappings,  $\chi_\alpha : \Omega_0 \rightarrow \Omega_t$ , for  $\alpha = s, f$ , such that

$$\mathbf{x} = \mathbf{x}_\alpha = \chi_\alpha(\mathbf{X}_\alpha, t). \quad (2)$$

Then, we can find the corresponding material points  $\mathbf{X}_\alpha$  in the undeformed configuration, via

$$\mathbf{X}_\alpha = \chi_\alpha^{-1}(\mathbf{x}_\alpha) \in \Omega_0. \quad (3)$$

In general,  $\mathbf{X}_s \neq \mathbf{X}_f$ . The displacement field is thus defined by

$$\mathbf{u}_\alpha = \mathbf{x}_\alpha - \mathbf{X}_\alpha. \quad (4)$$

Another important concept is the deformation gradient tensor, which is given by

$$\mathbf{F}_\alpha = \frac{\partial \mathbf{X}_\alpha}{\partial \mathbf{X}_\alpha}. \quad (5)$$

More importantly, the solid deformation tensor can be written as  $\mathbf{F}_s = \nabla_S \chi_s$ , where we have used  $\nabla_S$  to denote taking the partial derivative with respect to  $\mathbf{X}_s$  in the undeformed configuration,  $\Omega_0$ . For the rest of the paper, we adopt the notation  $\nabla = \nabla_x$  to indicate taking the partial derivative with respect to  $\mathbf{x}$  in the current configuration,  $\Omega_t$ .

## 2.2. Conservation of mass

The mass balance relations of the biphasic material, for each phase, are

$$\frac{\partial}{\partial t} (\rho_\alpha \phi_\alpha) + \nabla \cdot (\rho_\alpha \phi_\alpha \mathbf{v}_\alpha) = \tilde{q}_\alpha, \text{ in } \Omega_t, \quad (6)$$

where  $\alpha = s$  or  $f$ ,  $\rho_\alpha$  is the density,  $\mathbf{v}_\alpha = \partial \chi_\alpha / \partial t$  is the velocity, and  $\tilde{q}_\alpha$  is the external mass injection. We further assume that the fluid and solid phases are incompressible. It is worth noting that only fluid is injected in the tissue, so  $\tilde{q}_s = 0$ . Then, the conservation of mass can be reduced to the following,

$$\nabla \cdot \mathbf{v}_s + \nabla \cdot (\phi_f (\mathbf{v}_f - \mathbf{v}_s)) = \hat{q}_f, \text{ in } \Omega_t, \quad (7)$$

where  $\hat{q}_f = \tilde{q}_f / \rho_f$ . By introducing the seepage or Darcy velocity

$$\mathbf{w} := \phi_f (\mathbf{v}_f - \mathbf{v}_s), \quad (8)$$

and using the result in [40][Proposition 5.4], we can rewrite Eq. (7) as

$$\frac{1}{J_s} \frac{dJ_s}{dt} + \nabla \cdot \mathbf{w} = \hat{q}_f, \text{ in } \Omega_t, \quad (9)$$

where  $J_s = \det(\mathbf{F}_s)$  is the Jacobian determinant, and  $d(\cdot)/dt$  represents taking the material derivative of  $(\cdot)$ .

## 2.3. Conservation of momentum

Neglecting acceleration terms, we formulate the conservation of momentum of each phase as

$$\nabla \cdot \boldsymbol{\sigma}^\alpha + \mathbf{f}_\alpha = \mathbf{b}_\alpha, \text{ in } \Omega_t, \quad (10)$$

where  $\boldsymbol{\sigma}^\alpha$  is the Cauchy stress tensor,  $\mathbf{b}_\alpha$  is the body force,  $\mathbf{f}_s$  is the force that the fluid phase acts on the solid phase and  $\mathbf{f}_f$  is the force that the solid phase exerts on the fluid phase. By Newton's third law, we have  $\mathbf{f}_f + \mathbf{f}_s = \mathbf{0}$ . Summing up the two conservation of momentum equations, we obtain,

$$\nabla \cdot \boldsymbol{\sigma}^{\text{por}} = \mathbf{0}, \text{ in } \Omega_t, \quad (11)$$

where  $\boldsymbol{\sigma}^{\text{por}} = \boldsymbol{\sigma}^s + \boldsymbol{\sigma}^f$ , and we have assumed  $\mathbf{b}_\alpha = \mathbf{0}$ .

## 2.4. Constitutive law for the fluid flow

We assume the fluid flow relative to the solid phase follows Darcy's law, and the fluid is a Newtonian fluid. Then, the Darcy velocity defined in Eq. (8) can be written as

$$\mathbf{w} = \phi_f (\mathbf{v}_f - \mathbf{v}_s) = -\frac{k}{\mu_f} (\nabla p - \rho_f \mathbf{g}), \quad (12)$$

where  $k$  is the permeability of the tissue,  $\mu_f$  is the fluid viscosity and is assumed to be constant in this work,  $p$  is the pore pressure, and  $\mathbf{g}$  is the body force per unit mass due to gravity.

The pore structure of the porous medium changes as the tissue deforms, and the permeability,  $k$ , changes accordingly. In linear poro-elasticity, the permeability  $k$  is assumed to be independent of the deformation because the deformation is too small to alter the pore structure. However, in nonlinear poro-elasticity, it is more appropriate

to model permeability as a function of the finite solid deformation [37]. For simplicity, we choose the normalized Kozeny–Carman formula, given by

$$k(\phi_f) = k_0 \frac{(1 - \phi_{f,0}^2)^2}{\phi_{f,0}^3} \frac{\phi_f^3}{(1 - \phi_f)^2}, \tag{13}$$

where  $\phi_{f,0} = \phi_f(\mathbf{x}, 0)$  is the initial (undeformed) porosity, and  $k_0 = k(\phi_{f,0})$  is the initial permeability. The well-posedness of the Kozeny–Carman formula used for linear kinematic poro-elastic models is shown in [41,42]. It is worth noting that Eq. (13) also takes into account the case of small enough deformation that does not change the pore structure, i.e., if  $\phi_f = \phi_{f,0}$ ,  $k = k_0$ , so the Kozeny–Carman formula is used for both the linear and nonlinear poro-elastic models in this work. We remark that the volume fraction of the fluid (also called porosity) can be obtained through the saturation constraint Eq. (1) and the Jacobian determinant,

$$\phi_f = 1 - \phi_s = 1 - \frac{\phi_{s,0}}{J_s}, \tag{14}$$

where  $\phi_{s,0}$  is the undeformed volume fraction of the solid.

### 2.5. Constitutive law for the solid

Recall that the overall Cauchy stress of the tissue, Eq. (11), consists of the fluid ( $\sigma^f$ ) and solid ( $\sigma^s$ ) contributions. We neglect the shear component of the fluid and approximate the Cauchy stress of the fluid contribution [39] by

$$\sigma^f \approx -\phi_f p \mathbf{I}, \tag{15}$$

where  $\mathbf{I}$  is the  $d \times d$  identity matrix. The Cauchy stress of the solid phase is defined in terms of the elastic stress  $\sigma_E^s$  and pore pressure  $p$ , as

$$\sigma^s = \sigma_E^s - \phi_s p \mathbf{I}. \tag{16}$$

By adding Eqs. (15) and (16), we have the Cauchy stress of the tissue as

$$\sigma^{\text{por}} = \sigma_E^s - p \mathbf{I}, \tag{17}$$

where we have used Eq. (1). Next, we introduce two constitutive laws (linear elasticity and the Ogden hyperelasticity) for the elastic stress,  $\sigma_E^s$ .

#### 2.5.1. Linear elasticity

The solid deformation can be modeled using linear elasticity if the tissue deformation is infinitesimal. We discuss briefly the infinitesimal deformation assumption herein for completeness and detailed derivation of linear poro-elasticity can be found in [37].

**Assumption 2.1.** If the deformation of the material is small, such that,

$$\frac{\|\mathbf{u}_s\|}{\text{diam}(\Omega_t)} \approx \|\nabla \mathbf{u}_s\| \ll 1, \tag{18}$$

where we have abused the notations for the vector and tensor norms, and used  $\|\cdot\|$  to denote any pair of norms compatible for the given vector and tensor, then, the current and undeformed configurations overlap ( $\Omega_t = \Omega_0$ ), so  $\nabla_S = \nabla = \nabla_{\mathbf{x}}$ . Moreover, the Jacobian determinant is approximated [39] by

$$J_s \approx \tilde{J}_s = 1 + \nabla \cdot \mathbf{u}_s. \tag{19}$$

Under Assumption 2.1, the linearized Cauchy stress tensor is given by

$$\sigma_E^s \approx \sigma_{LE}^s = 2\mu \boldsymbol{\epsilon} + \lambda \text{tr}(\boldsymbol{\epsilon}) \mathbf{I}, \tag{20}$$

where  $\mu$  and  $\lambda$  are Lamé coefficients,  $\text{tr}(\cdot)$  is the trace operator, and  $\boldsymbol{\epsilon}$  is the symmetric linear elastic strain tensor, defined as

$$\boldsymbol{\epsilon}(\mathbf{u}_s) = \frac{1}{2} (\nabla \mathbf{u}_s + \nabla \mathbf{u}_s^T). \tag{21}$$

### 2.5.2. The Ogden hyperelasticity

For finite deformation, we adopt the Ogden hyperelasticity model, which is commonly used to model soft tissue [10,22–26,43], with an extension term accounting for the volumetric deformation [10]. The strain–energy function of the solid can be split into isochoric and volumetric parts

$$\Psi^s = \Psi^{\text{Ogd}} + U(J_s), \tag{22}$$

where  $\Psi^{\text{Ogd}}$  is the Ogden strain–energy function that is isochoric, and  $U(J_s)$  is an extensional function [38], which describes the compressibility effects of the tissue, and is given as

$$U(J_s) = \lambda(1 - \phi_{s,0}^2) \left[ \frac{J_s - 1}{1 - \phi_{s,0}} - \ln \left( \frac{J_s - \phi_{s,0}}{1 - \phi_{s,0}} \right) \right]. \tag{23}$$

The isochoric Ogden strain–energy function [44] is defined by

$$\Psi^{\text{Ogd}} = \sum_{i=1}^3 \frac{\mu_i}{\alpha_i} [\tilde{\lambda}_1^{\alpha_i} + \tilde{\lambda}_2^{\alpha_i} + \tilde{\lambda}_3^{\alpha_i} - 3], \tag{24}$$

where  $\mu_i$  and  $\alpha_i$  are positive constitutive parameters that are identified in experiments,  $\tilde{\lambda}_a$ , for  $a = 1, 2, 3$ , is the isochoric principal stretch, which is defined by  $\tilde{\lambda}_a = \lambda_a J_s^{-1/3}$ , where  $\lambda_a$  is called the principal stretch and is defined through the left Cauchy–Green deformation tensor,

$$\mathbf{B}_s = \mathbf{F}_s \mathbf{F}_s^T = \sum_{a=1}^3 \lambda_a^2 \hat{\mathbf{n}}_a \otimes \hat{\mathbf{n}}_a, \tag{25}$$

where  $\hat{\mathbf{n}}_a$  is the normalized eigenvector of  $\mathbf{B}_s$ , and  $\lambda_a^2$  is the corresponding eigenvalue. The shear modulus can be obtained through

$$\mu = \frac{1}{2} \sum_{i=1}^3 \mu_i \alpha_i. \tag{26}$$

Then, the Cauchy stress tensor is obtained by

$$\boldsymbol{\sigma}_E^s = \frac{\boldsymbol{\tau}_E^s}{J_s}, \tag{27}$$

where  $\boldsymbol{\tau}_E^s$  is the Kirchhoff extra stress tensor,

$$\boldsymbol{\tau}_E^s = \mathbf{F}_s \left( 2 \frac{\partial \Psi^s}{\partial \mathbf{C}_s} \right) \mathbf{F}_s^T = 2 \frac{\partial \Psi^s}{\partial \mathbf{B}_s} \mathbf{B}_s, \tag{28}$$

where  $\mathbf{C}_s$  is the right Cauchy–Green deformation tensor, i.e.,

$$\mathbf{C}_s = \mathbf{F}_s^T \mathbf{F}_s. \tag{29}$$

Using Eqs. (22)–(24) and (28), we arrive at the Kirchhoff extra stress tensor,

$$\boldsymbol{\tau}_E^s = \boldsymbol{\tau}_E^{\text{Ogd}} + \boldsymbol{\tau}_E^{\text{vol}}, \tag{30}$$

where  $\boldsymbol{\tau}_E^{\text{vol}}$  is the volumetric part, given as

$$\boldsymbol{\tau}_E^{\text{vol}} = \mathbf{F}_s \left( 2 \frac{\partial U}{\partial \mathbf{C}_s} \right) \mathbf{F}_s^T = \bar{\tau}_E^{\text{vol}} \mathbf{I}, \tag{31}$$

with

$$\bar{\tau}_E^{\text{vol}} = \lambda(1 - \phi_{s,0}^2) \left( \frac{J_s}{1 - \phi_{s,0}} - \frac{J_s}{J_s - \phi_{s,0}} \right), \tag{32}$$

and the isochoric part is given by

$$\boldsymbol{\tau}_E^{\text{Ogd}} = 2 \frac{\partial \Psi^s}{\partial \mathbf{B}_s} \mathbf{B}_s = \sum_{a=1}^3 \beta_a \hat{\mathbf{n}}_a \otimes \hat{\mathbf{n}}_a, \tag{33}$$

where  $\beta_a$  is obtained using

$$\beta_a = \sum_{i=1}^3 \mu_i \left[ \tilde{\lambda}_a^{\alpha_i} - \frac{1}{3} (\tilde{\lambda}_1^{\alpha_i} + \tilde{\lambda}_2^{\alpha_i} + \tilde{\lambda}_3^{\alpha_i}) \right]. \tag{34}$$

### 2.6. Poro-elasticity

We summarize in this subsection the two poro-elastic models, linear poro-elasticity and nonlinear poro-hyperelasticity, which are used to model the poro-elastic response of subcutaneous tissue during injection.

#### 2.6.1. Linear poro-elasticity

If Assumption 2.1 is satisfied, by collecting Eqs. (9), (11) and (20) and using Eq. (19), we obtain the governing equations of the linear poro-elastic model, for incompressible fluid and solid, as

$$\begin{cases} \nabla_S \cdot (\sigma_{LE}^s - p\mathbf{I}) & = \mathbf{0}, \text{ in } \Omega_0 \times (0, T], \\ \frac{\partial}{\partial t} (\nabla_S \cdot \mathbf{u}_s) + \nabla_S \cdot \mathbf{w} & = \hat{q}_f, \text{ in } \Omega_0 \times (0, T], \end{cases} \tag{35}$$

Recall that Eq. (19) in Assumption 2.1 serves as an indicator of whether linear poro-elasticity is adequate to model subcutaneous injection. We quantify the deformation using the Jacobian determinant ( $\|J_s\|_{L^p(\bar{\Omega})}$ ) and its approximation error ( $\|J_s - \tilde{J}_s\|_{L^p(\bar{\Omega})}$ ), and validate the infinitesimal deformation assumption using numerical solutions in Section 5.2. We remark that we have abused the notation  $p \geq 1$  here to denote the classical Lebesgue space  $L^p(\bar{\Omega})$  equipped with the norm  $\|\cdot\|_{L^p(\bar{\Omega})}$ . The domain  $\bar{\Omega}$  is not necessarily equal to  $\Omega_0$  and will be addressed later along with the choice of the Lebesgue space  $L^p$ .

#### 2.6.2. Nonlinear poro-hyperelasticity

Combining Eqs. (9), (11) and (27), we obtain the nonlinear poro-hyperelasticity model equations

$$\begin{cases} \nabla \cdot \sigma^{\text{por}} & = \mathbf{0}, \text{ in } \Omega_t, \\ \frac{1}{J_s} \frac{dJ_s}{dt} + \nabla \cdot \mathbf{w} & = \hat{q}_f, \text{ in } \Omega_t, \end{cases} \tag{36}$$

where  $\sigma^{\text{por}}$  is given by Eq. (17).

For the rest of the paper, we refer to Eq. (35) as the linear model and Eq. (36) as the nonlinear model. We summarize the major differences of the linear and nonlinear models in the following remark.

#### Remark 2.2.

- i. The kinematics of the material: the balance laws of the linear model are established based on the infinitesimal deformation assumption, while that of the nonlinear model is valid for finite deformation.
- ii. The solid constitutive law: the stress–strain constitutive relation of the solid material in the linear model is modeled via linear elasticity, while the nonlinear model uses the Ogden hyperelastic model.

### 3. Numerical methods

In this section, we discuss temporal and spatial discretizations used in this work. The numerical procedure is implemented using the open source finite element library deal.II [10,45–50].

#### 3.1. Temporal discretization

We use the backward Euler scheme for temporal discretization,

$$\frac{dJ_s}{dt} \approx \frac{J_s^n - J_s^{n-1}}{\Delta t}, \tag{37}$$

where we have denoted by  $\Delta t = t^n - t^{n-1}$  the uniform time increment between time  $t^n$  and  $t^{n-1}$ , for  $n \geq 1$ , and the superscripts  $(\cdot)^n$  and  $(\cdot)^{n-1}$  denote the respective values at these time instances.

### 3.2. Spatial discretization

Let  $\mathcal{T}_h$  be a conforming, shape-regular, quasi-uniform triangulation of the undeformed configuration  $\Omega_0$ , consisting of polyhedrons in 3D. The finite element space for solid displacement  $\mathbf{u}_s$  is denoted as

$$\mathbf{V}_h^{r_0} := \left\{ \mathbf{v} \in [H^1(\Omega_0)]^d : \mathbf{v}|_{\Omega_e} \in [\mathbb{P}_r(\Omega_e)]^d, \forall \Omega_e \in \mathcal{T}_h, \mathbf{v}|_{\Gamma_D^{u_s}} = \mathbf{0} \right\}, \text{ for } r_0 = 1, 2, \tag{38}$$

where  $H^1$  is the standard Sobolev space,  $\mathbb{P}_r$  denotes polynomials of order  $r_0$ , and  $\Gamma_D^{u_s} \subset \partial\Omega_0$  is the Dirichlet boundary of the solid displacement. The discrete space for pore pressure  $p$  is

$$\mathcal{Q}_h := \left\{ \theta \in H^1(\Omega_0) : \theta|_{\Omega_e} \in \mathbb{P}_1(\Omega_e), \forall \Omega_e \in \mathcal{T}_h, \theta|_{\Gamma_D^p} = 0 \right\}, \tag{39}$$

where  $\Gamma_D^p \subset \partial\Omega_0$  is the Dirichlet boundary of pore pressure.

We adopt an iterative procedure namely, the fixed-stress split, which is widely used for linear poro-elasticity, to solve both the linear and nonlinear models, Eqs. (35) and (36) with appropriate boundary conditions. The fixed-stress scheme solves the poro-elastic equations in an iterative manner, namely, the conservation of mass (or momentum) is solved first with a fixed constant mean stress, and the conservation of momentum (or mass) is solved afterwards, until a tolerance is achieved. Linear poro-elasticity with fixed-stress split has been studied extensively, and we refer readers to [30,31,51] for details. We present the fixed-stress split of the nonlinear poro-elastic model in the next section.

## 4. Fixed-stress split for the nonlinear poro-elastic model

The fixed-stress split of the linear poro-elastic model enables the use of different solvers and preconditioners for the conservation of mass and momentum equations [52,53], and is proved to be stable and convergent [28–31,51]. However, previous studies have used a monolithic solver [10,33] or  $L$ -scheme [34] to solve the nonlinear poro-elastic model.

In this section, we present the fixed-stress split for the nonlinear poro-elastic model. We start with the fixed-stress split in the continuous form, and proceed with the presentation of the discrete formulation. Convergence properties of the fixed-stress split under spatial and temporal refinements are demonstrated using numerical examples. Finally, solutions of the fixed-stress split and a monolithic solver are compared.

### 4.1. Continuous formulation of the fixed-stress split

The key idea of the fixed-stress split is to identify the volumetric mean stress and assume the volumetric mean stress is constant between two iterations. The split of the strain–energy function into isochoric and volumetric parts, as shown in Eq. (22), facilitates the extension of the fixed-stress iterative scheme to nonlinear poro-elastic models. We define the volumetric mean stress of the nonlinear model, as

$$\bar{\sigma}_v = \bar{\sigma}_v^0 + \bar{\sigma}_E^{\text{vol}} - (\bar{\sigma}_E^{\text{vol}})^0 - (p - p^0), \tag{40}$$

where we have used the superscripts,  $(\cdot)^0$ , to denote the respective values at  $t = 0$ , and  $\bar{\sigma}_E^{\text{vol}}$  is defined using Eq. (32), i.e.,

$$\bar{\sigma}_E^{\text{vol}} = \frac{\bar{\tau}_E^{\text{vol}}}{J_s} = \lambda(1 - \phi_{s,0}^2) \left( \frac{1}{1 - \phi_{s,0}} - \frac{1}{J_s - \phi_{s,0}} \right). \tag{41}$$

Taking the material time derivative of  $\bar{\sigma}_E^{\text{vol}}$ , we have

$$\frac{d(\bar{\sigma}_v + p)}{dt} = \frac{d(\bar{\sigma}_E^{\text{vol}})}{dt} = \frac{1}{\beta(J_s)} \frac{dJ_s}{dt}, \tag{42}$$

where

$$\beta(J_s) = \frac{(J_s - \phi_{s,0})^2}{\lambda(1 - \phi_{s,0})^2}. \tag{43}$$

It is worth mentioning that  $\beta(J_s)$  can also be written as  $\beta(\mathbf{u})$  because  $J_s = J_s(\mathbf{u})$ .

Following [31], we assume constant volumetric mean stress. Namely,  $\bar{\sigma}_v$ , defined in Eq. (40), is kept constant between two iterative steps. So that,  $(\bar{\sigma}_v)^l = (\bar{\sigma}_v)^{l-1}$ , where  $l \geq 1$  is the iterative step. The iterative procedure reads as follows:

$$\begin{aligned} \frac{\beta(\mathbf{u}^{l-1})}{J_s(\mathbf{u}^{l-1})} \frac{dp^l}{dt} + \nabla \cdot \mathbf{w}(p^l, \mathbf{u}^{l-1}) &= -\frac{\beta(\mathbf{u}^l)}{J_s(\mathbf{u}^l)} \frac{d\bar{\sigma}_v^l}{dt} + \hat{q}_f \\ &= -\frac{\beta(\mathbf{u}^{l-1})}{J_s(\mathbf{u}^{l-1})} \frac{d}{dt} \left[ (\bar{\sigma}_E^{\text{vol}})^{l-1} - p^{l-1} \right] + \hat{q}_f, \text{ in } \Omega_t, \end{aligned} \tag{44a}$$

$$\nabla \cdot \boldsymbol{\sigma}^{\text{por}}(\mathbf{u}^l, p^l) = \mathbf{0}, \text{ in } \Omega_t. \tag{44b}$$

We remark that the fixed-stress iterative method splits the nonlinear poro-elastic model, Eq. (36), into a system consisting of a linear equation (44a) and a nonlinear (44b) equation. Thus, Eqs. (44a) and (44b) can be solved separately while Eq. (36) has to be solved in a monolithic fashion. Moreover, the fixed-stress split is general to any nonlinear poro-elastic model. The key of the fixed-stress split is to identify the volumetric mean stress which requires the splitting of the strain–energy function into the isochoric and volumetric contributions.

#### 4.2. Discrete formulation of the fixed-stress split

Using the spatial and temporal discretizations introduced in Section 3, we present the weak form of Eq. (44). The fixed-stress split for nonlinear poro-elastic models is carried out as follows. We first solve the equation of conservation of mass, given  $\mathbf{u}_{s,h}^{n,l-1}$ , find  $p_h^{n,l} \in \mathcal{Q}_h$  such that,

$$\begin{aligned} \int_{\Omega_t} \frac{\beta^{n,l-1}}{J_s^{n,l-1} \Delta t} p_h^{n,l} \theta_h d\Omega_t - \int_{\Omega_t} \mathbf{w}^{n,l} \cdot \nabla \theta_h d\Omega_t &= \int_{\Omega_t} \frac{\beta^{n,l-1}}{J_s^{n,l-1} \Delta t} p_h^{n-1} \theta_h d\Omega_t \\ - \int_{\Omega_t} \frac{\beta^{n,l-1}}{J_s^{n,l-1}} \left( \frac{(\bar{\sigma}_E^{\text{vol}})^{n,l-1} - (\bar{\sigma}_E^{\text{vol}})^{n-1}}{\Delta t} - \frac{p_h^{n,l-1} - p_h^{n-1}}{\Delta t} \right) \theta_h d\Omega_t & \\ + \int_{\Omega_t} \hat{q}_f \theta_h d\Omega_t, \quad \forall \theta_h \in \mathcal{Q}_h, \end{aligned} \tag{45}$$

where  $\beta^{n,l-1} = \beta(J_s^{n,l-1})$ . The equation of conservation of momentum is solved next: given  $p_h^{n,l}$ , find  $\mathbf{u}_{s,h}^{n,l} \in \mathcal{V}_h$  such that

$$\int_{\Omega_t} \boldsymbol{\sigma}^{\text{por}}(\mathbf{u}_{s,h}^{n,l}, p_h^{n,l}) : \nabla \mathbf{v}_h d\Omega_t = 0, \quad \forall \mathbf{v}_h \in \mathcal{V}_h^{r0}. \tag{46}$$

We iterate this procedure, namely, solving Eqs. (45) and (46) successively, until [30,51]

$$\left\| \frac{\bar{\sigma}_v^{n,l} - \bar{\sigma}_v^{n,l-1}}{\lambda} \right\|_{L^\infty} \leq \text{TOL}_{FS}, \quad \text{TOL}_{FS} > 0, \tag{47}$$

where  $\text{TOL}_{FS}$  is the tolerance. Alternatively, for  $\|\mathbf{u}_s^{n,l-1}\|_{L^2(\Omega_t)} \neq 0$  and  $\|p^{n,l-1}\|_{L^2(\Omega_t)} \neq 0$ ,

$$\max \left\{ \frac{\|\mathbf{u}_s^{n,l} - \mathbf{u}_s^{n,l-1}\|_{L^2(\Omega_t)}}{\|\mathbf{u}_s^{n,l-1}\|_{L^2(\Omega_t)}}, \frac{\|p^{n,l} - p^{n,l-1}\|_{L^2(\Omega_t)}}{\|p^{n,l-1}\|_{L^2(\Omega_t)}} \right\} \leq \text{TOL}_{FS}, \tag{48}$$

can also be used as the stopping criterion [52,54]. The conservation of mass, Eq. (45), is linear in terms of pore pressure, and Conjugate Gradient solver with algebraic multigrid preconditioner is used. The conservation of momentum, Eq. (46), is highly nonlinear and Newton–Raphson iterative method with line search [54] is adopted. We use the automatic differentiation package *Sacado* [55] provided by *Trilinos* to construct the Jacobian matrix and the resulting linear system is solved using the direct solver. A summary of the fixed-stress algorithm is presented in Algorithm 1.

#### 4.3. Convergence of the fixed-stress split under spatial and temporal refinements

In this section we study the convergence properties of the fixed-stress split under spatial ( $h$ ) and temporal ( $t$ ) refinements. Because analytical solutions of the nonlinear model are not available, we instead simulate the unconfined compression test of human adipose tissue as in [26].

---

**Algorithm 1:** Fixed-stress split for the nonlinear poro-elastic model

---

At each time  $t^n$ , for  $n \geq 1$

Set  $\mathbf{u}_{s,h}^{n,0} = \mathbf{u}_{s,h}^{n-1}$ ,  $p_h^{n,0} = p_h^{n-1}$ .

**Repeat:** for  $l \geq 1$

Solve the conservation of mass, Eq. (45).

Solve the conservation of momentum, Eq. (46).

**Until:**

Eqs. (47) or (48) is satisfied.

Set  $\mathbf{u}_{s,h}^n = \mathbf{u}_{s,h}^{n,l}$ ,  $p_h^n = p_h^{n,l}$ .

Increment  $t^n \rightarrow t^{n+1}$ .

---

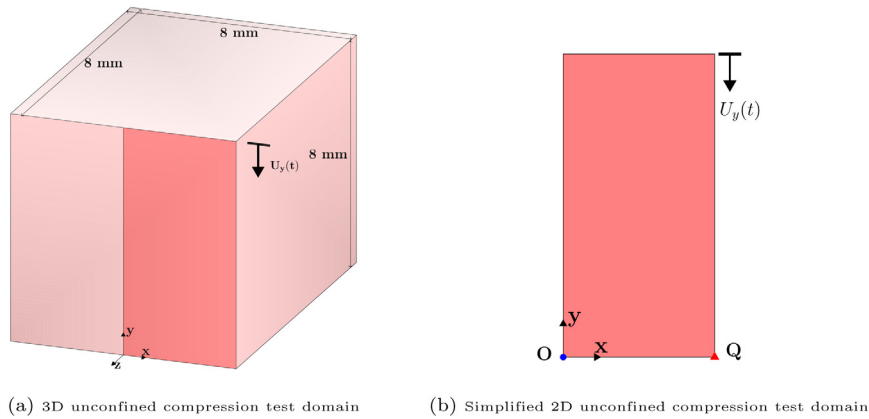


**Fig. 1.** (a): Three-dimensional unconfined compression test domain [26]. The top surface is subjected to a displacement loading  $U_y(t)$ . (b): Simplified two-dimensional unconfined compression test domain represented as in the dark red area in (a). The coordinates of the points **O** (blue circle) and **Q** (red triangle) are  $(0, 0)$  and  $(4 \text{ mm}, 0)$ , respectively.

The three-dimensional cubic human adipose tissue sample is modeled as shown in Fig. 1(a). In the  $y$  direction, the top surface ( $y = 8 \text{ mm}$ ) is subjected to a displacement loading (the strain rate is  $3 \text{ s}^{-1}$ ), and the bottom surface ( $y = 0$ ) is confined. Under compression, the sample is free to expand in the  $x$  and  $z$  directions, and the fluid can exit the tissue through the surfaces,  $x = \pm 4 \text{ mm}$ , and  $z = 0$  and  $-8 \text{ mm}$ . We simplify the three-dimensional compression test using a two-dimensional compression problem as shown in Fig. 1(b).

The boundary conditions of the simplified compression problem are summarized below,

$$\begin{cases} \nabla p \cdot \mathbf{n} = 0, & \mathbf{u}_s \cdot \mathbf{n} = 0, \sigma^{\text{por}} \mathbf{n} \cdot \mathbf{e}_y = 0, & \text{on } x = 0, \\ p = 0, & \sigma^{\text{por}} \mathbf{n} = \mathbf{0}, & \text{on } x = 4 \text{ mm}, \\ \nabla p \cdot \mathbf{n} = 0, & \mathbf{u}_s \cdot \mathbf{n} = 0, \sigma^{\text{por}} \mathbf{n} \cdot \mathbf{e}_x = 0, & \text{on } y = 0, \\ \nabla p \cdot \mathbf{n} = 0, & \mathbf{u}_s \cdot \mathbf{n} = U_y(t), \sigma^{\text{por}} \mathbf{n} \cdot \mathbf{e}_x = 0, & \text{on } y = 8 \text{ mm}, \end{cases} \quad (49)$$

where  $\mathbf{n}$  is the unit normal vector pointing outward of the face,  $\mathbf{e}_i$ , for  $i = x, y$  is the unit vector in the  $i$ th direction, and the displacement loading is given as

$$U_y(t) = -24t \text{ mm}, \quad t \leq \frac{2}{15} \text{ s}. \quad (50)$$

The Ogden hyperelastic model parameters in Eq. (24) are taken from [26], as

$$\mu_1 = 0.601 \text{ kPa}, \mu_2 = \mu_3 = 0, \text{ and } \alpha_1 = 13.353, \alpha_2 = \alpha_3 = 1, \quad (51)$$

then the Lamé constants are obtained through  $\lambda = 2\mu\nu/(1 - 2\nu)$ , where  $\mu$  is from Eq. (26). We choose  $\nu = 0.49$ ,  $\phi_{f,0} = 0.1$ , and  $k_0 = 1 \text{ D}$ , where  $\text{D}$  is the Darcy unit. We use linear elements ( $\mathbf{V}_h^1 \times \mathbf{Q}_h$ ) for both pressure and

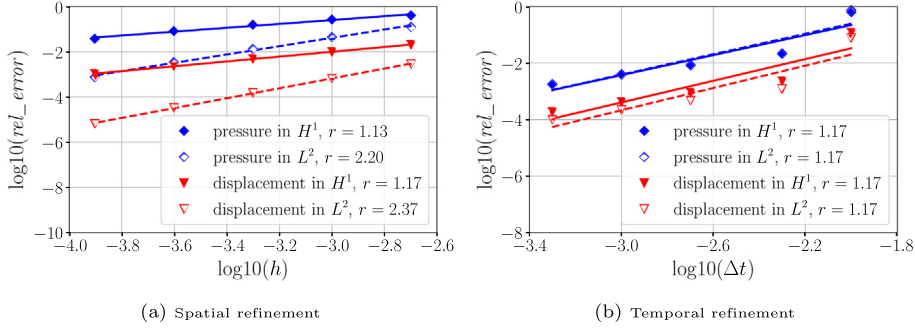


**Fig. 2.** Convergence results of the fixed-stress iteration. *rel\_error* represents the relative error against the reference solution. The convergence rates are denoted as *r* in the legend and the values are the slope between the finest (spatial or temporal) two data points. The reference solution is obtained using a mesh of  $2^6 \times 2^7$  elements and a time step of  $\Delta t = 0.0001$  s.

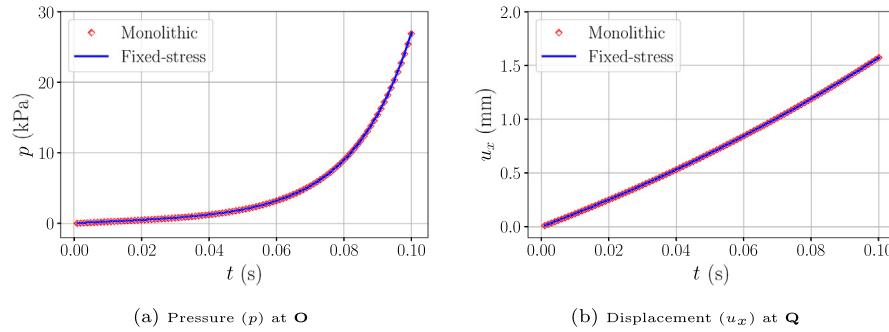


**Fig. 3.** Comparison of the pore pressure (*p*) and the first component of the displacement (*u<sub>x</sub>*) using the fixed-stress split and the monolithic methods. The time step is  $\Delta t = 0.001$  s, and the initial domain is uniformly discretized into  $2^5 \times 2^6$  elements.

displacements. The tolerance of the fixed-stress split,  $TOL_{FS}$  in Algorithm 1, is set to be  $1.0 \times 10^{-10}$  and this applies to all numerical examples in this section. The compression problem is simulated for a total of 0.1 s, and the strain level reaches 30% at  $T = 0.1$  s. The relative errors in  $L^2$  and  $H^1$  norms of the displacement and pressure are evaluated at  $T = 0.1$  s.

For spatial refinement, the domain shown in Fig. 1(b) is discretized into  $2^n \times 2^{n+1}$  elements, for  $n = 1, 2, \dots, 6$ . The time step is chosen to be  $\Delta t = 0.0001$  s. The solutions obtained from the finest mesh ( $n = 6$ ) are treated as the reference solution. The displacement and pressure error of the coarse meshes ( $n < 6$ ) are calculated against the reference solution. The convergence profiles are presented in Fig. 2(a). Second-order convergence rates are observed for both the pressure and displacement in  $L^2$  norm, while first-order convergence rates are obtained in  $H^1$  norm. The convergence rates under *h*-refinement are optimal with respect to the chosen trial and test function spaces.

For temporal refinement, the mesh consists of  $2^6 \times 2^7$  elements. We compare the solutions using  $\Delta t = 0.01, 0.005, 0.002, 0.001, 0.005$  s against that of  $\Delta t = 0.0001$  s. Convergence profiles of the displacement and pore pressure are shown in Fig. 2(b). First-order convergence rates are recovered for both variables in  $L^2$  and  $H^1$  norms, and this agrees with the optimal convergence rate of the implicit Euler method introduced in Section 3.1.

In addition, we solve the two-dimensional compression problem using the proposed fixed-stress split and the monolithic method. The initial mesh is uniformly discretized into  $2^5 \times 2^6$  elements and the time step is  $\Delta t = 0.001$  s. Fig. 3 indicates that the pore pressure at O and the first component of the displacement (*u<sub>x</sub>*) at Q, are in good match. The number of iterations using the two stopping criteria Eqs. (47) and (48), are similar and are reported in Fig. 4.

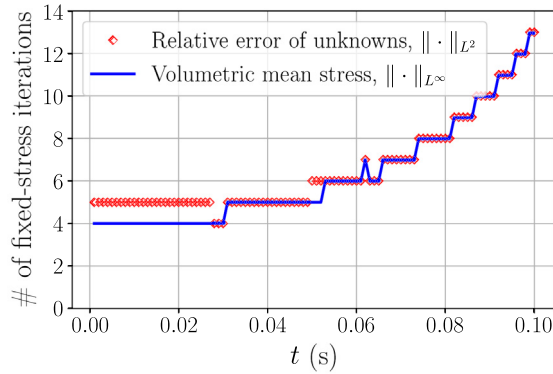


**Fig. 4.** Number of fixed-stress iterations using different stopping criteria, Eqs. (47) and (48). The time step is  $\Delta t = 0.001$  s, and the initial domain is uniformly discretized into  $2^5 \times 2^6$  elements.

### 5. Application to subcutaneous injection

In this section, we apply the poro-elastic models Eqs. (35) and (36) to study subcutaneous injection. The modeling of the subcutaneous tissue is addressed first. Then, the numerical validation of the linear model is performed. Finally, the linear and nonlinear models with application to subcutaneous injection are compared.

#### 5.1. Tissue modeling

For simplicity, we assume the geometry of the subcutaneous tissue of interest is a rectangular prism. In the poro-elastic models, Eqs. (35) and (36), we model the drug injection as an external source ( $\hat{q}_f$ ), located on the centerline that is perpendicular to the top and bottom surfaces of the prism. Due to symmetry, it is sufficient to carry out the computation only on a quarter of the tissue. The initial quarter domain,  $\Omega_0 = (0, 0.1\text{m})^d$  as shown in Fig. 5, is chosen sufficiently large such that the effect of the boundary conditions on the numerical results is minimized. For the rest of the paper, we omit the unit in length scale and use meter (m) unless specified. The symmetry planes are  $x = 0$  and  $y = 0$ . The top surface ( $z = 0.1$ ), representing the skin surface, is impermeable for fluid flow but is subjected to deformation. The bottom surface ( $z = 0$ ) is fixed in position,  $\mathbf{u}_s = \mathbf{0}$ . The fluid is allowed to flow out of the domain from boundaries,  $x = 0.1$ ,  $y = 0.1$ , and  $z = 0$ , which are called the drained boundaries. The pressure values at the drained boundaries in human subcutaneous tissue are not available, thus we choose  $p = 0$  for convenience. The boundary conditions are summarized in Eq. (52).

$$\begin{cases} \nabla p \cdot \mathbf{n} = 0, & \boldsymbol{\sigma}^{\text{por}} \mathbf{n} = \mathbf{0}, & \text{on } x = 0, \\ p = 0, & \boldsymbol{\sigma}^{\text{por}} \mathbf{n} = \mathbf{0}, & \text{on } x = 0.1, \\ \nabla p \cdot \mathbf{n} = 0, & \boldsymbol{\sigma}^{\text{por}} \mathbf{n} = \mathbf{0}, & \text{on } y = 0, \\ p = 0, & \boldsymbol{\sigma}^{\text{por}} \mathbf{n} = \mathbf{0}, & \text{on } y = 0.1, \\ p = 0, & \mathbf{u}_s = \mathbf{0}, & \text{on } z = 0, \\ \nabla p \cdot \mathbf{n} = 0, & \boldsymbol{\sigma}^{\text{por}} \mathbf{n} = \mathbf{0}, & \text{on } z = 0.1, \end{cases} \quad (52)$$

where  $\mathbf{n}$  is the unit outward normal vector.

As shown in Fig. 5, the domain  $\Omega_0$  is initially discretized uniformly into  $10 \times 10 \times 10$  elements. We only refine the region (right in Fig. 5,  $0.02 \times 0.02 \times 0.02$  m<sup>3</sup> in size) near the injection site in order to reduce the computational cost. Recall that in Eq. (36), the source term,  $\hat{q}_f$ , is defined in the current configuration, it is difficult to track the volume of the injection because the tissue undergoes deformation and the volume of the tissue is unknown in prior. We use pullback operation and redefine the injection in the undeformed configuration, i.e., for  $T \geq 5$  s,

$$\int_0^T \int_{\Omega_t} \hat{q}_f(\mathbf{x}, t) d\Omega_t dt = \int_0^T \int_{\Omega_0} \hat{q}_f(\mathbf{x}, t) J_s d\Omega_0 dt = \int_0^T \int_{\Omega_0} \bar{q}_f(t) \chi_{\Omega_t^{\mathbf{B}}} d\Omega_0 dt, \quad (53)$$

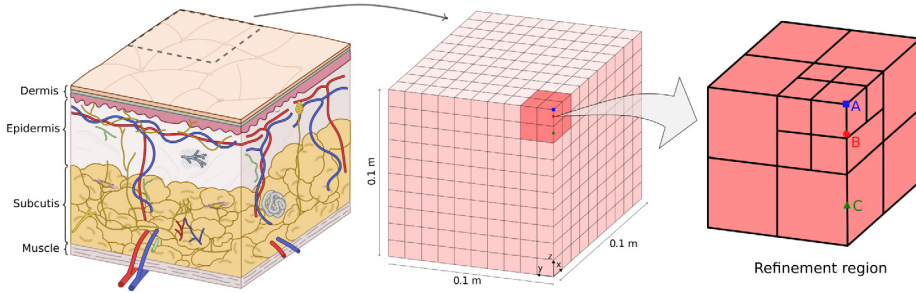


**Fig. 5.** (Left) Schematic view of the subcutaneous tissue. (Middle) Computational model ( $\Omega_0$ ) of a quarter of the tissue. (Right) Refinement region near the injection site,  $B$  (red circle),  $(0, 0, 0.096)$ , is the injection point,  $A$  (blue square),  $(0, 0, 0.1)$ , and  $C$  (green triangle),  $(0, 0, 0.085)$ , are observation points.

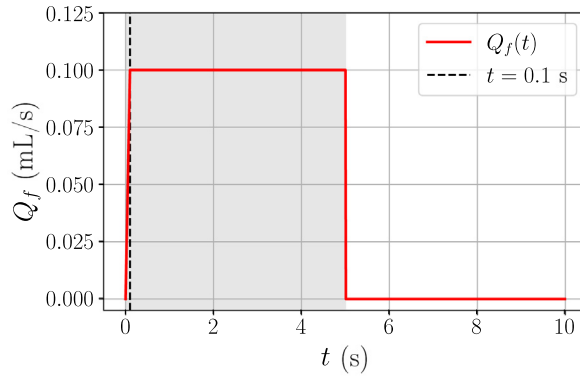


**Fig. 6.** Volumetric injection rate ( $Q_f(t)$ ) over time. The shaded area represents the injection process.

where we have defined  $\bar{q}_f(t)\chi_{\Omega_e^B} := \hat{q}_f(\mathbf{x}, t)J_s$ , and  $\chi_{\Omega_e^B}$  is the indicator function over  $\Omega_e^B \in \mathcal{T}_h$ , which is the element in the triangulation such that  $\mathbf{B} \in \Omega_e^B$  ( $\mathbf{B}$  is shown in Fig. 5 and our triangulation guarantees the uniqueness of  $\Omega_e^B$ ). Then, we have

$$\int_0^T \int_{\Omega_0} \bar{q}_f(t)\chi_{\Omega_e^B} d\Omega_0 dt = \int_0^T \bar{q}_f(t)|\Omega_e^B| dt = \int_0^T Q_f(t) dt = 0.495 \text{ mL}, \tag{54}$$

where  $|\Omega_e^B|$  is the measure (volume) of  $\Omega_e^B$ , and  $Q_f(t) := \bar{q}_f(t)|\Omega_e^B|$ , which is shown in Fig. 6. The total injection volume is 1.98 mL (0.495 mL for a quarter domain) over a duration of 5 s with an average injection rate of  $\approx 0.4$  mL/s. For  $t \in (0, 0.1)$  s,  $Q_f(t)$  increases linearly from 0 to 0.1 mL/s, stays constant from  $(0.1, 5)$  s, and finally drops to 0 after  $t > 5$  s.

**Remark 5.1.** The standard injection volume of subcutaneous delivery of mAbs is around 1–2 mL and more [5,7,56–58]. Self-administration of mAbs completes within seconds, thus the injection rate is around 0.1–0.5 mL/s. Such injection rate leads to the large deformation of the tissue and possibly invalidates the use of the linear model. Lower injection rate results in smaller deformation as shown in Appendix A.3.

For the rest of the section, the test and trial function spaces are taken to be  $V_h^1 \times Q_h$ , and the time step is  $\Delta t = 0.01$  s. The side and top views of the mesh at the refinement region, discussed in Fig. 5, are shown in Fig. 7, where 6 levels of refinement are used near the injection site  $\mathbf{B}$  with a minimum mesh size of 0.15625 mm. The typical subcutaneous injection needle sizes are 25–30 gauge [59] with inner diameters ranging from 0.15–0.25 mm. The refinement level is chosen such that the mesh size at the injection site represents the inner diameter of the needle. The mesh, which we call the coarse mesh, is fixed throughout the simulation. A fine mesh, Fig. A.10, near the injection site is also used and results are shown in Appendix A.1.

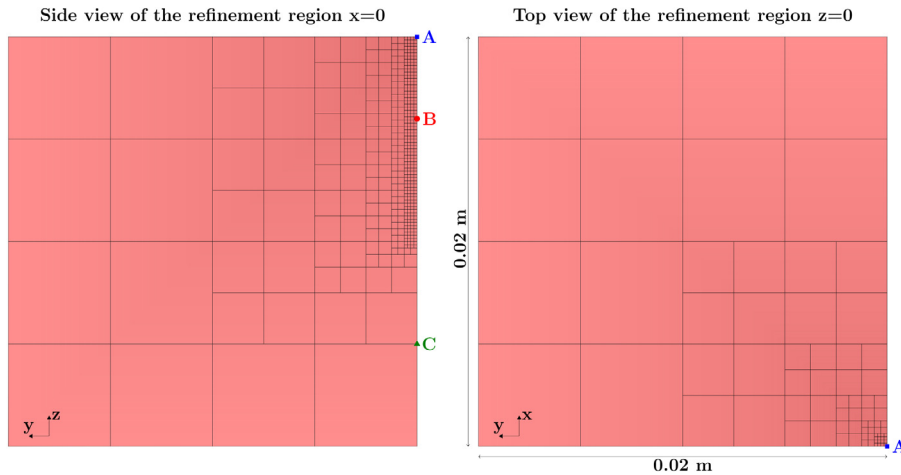


Fig. 7. Side and top views of the coarse mesh at the refinement region.

### 5.2. Numerical validation of the linear poro-elastic model

Linear poro-elasticity has been widely used in reservoir engineering [30,48,49,51], and is applied to subcutaneous injection in [14] without validation. The mechanical properties of the subcutaneous tissue are very different from those of the rock. The permeability of the adipose tissue and skin reported in experiments differ in several orders of magnitude (100 – 0.01 D) [6,60–63]. The Young’s modulus varies from 0.3–100 kPa [23,26,61,63]. Therefore, it is necessary to show if the linear poro-elastic model is still valid to study subcutaneous injection, for the wide range of material property values and injection rate.

Recall that both fluid and solid components are assumed to be incompressible. The unknown material parameters in the linear model are Lamé constants,  $\lambda$  and  $\mu$ , initial permeability,  $k_0$ , fluid viscosity,  $\mu_f$ , and initial porosity,  $\phi_0$ . We further assume that the tissue is homogeneous and isotropic with an initial porosity  $\phi_0 = 0.1$  and a Poisson ratio  $\nu = 0.49$ , and that the fluid viscosity is constant,  $\mu_f = 1$  cP. Then Lamé constants can be uniquely determined using Young’s modulus  $E$ , and Poisson ratio  $\nu$ , through  $\lambda = E\nu/((1 + \nu)(1 - 2\nu))$  and  $\mu = E/(2(1 + \nu))$ . It is worth noting that gravity is neglected for the rest of the paper.

We validate the linear model by studying the infinitesimal deformation Assumption 2.1 for the range of Young’s modulus and permeability values. From [14], we know that the solid deformation is significant only during the injection process, hence it is sufficient to study  $\|J_s\|_{L^p(\bar{\Omega})}$  and  $\|J_s - \tilde{J}_s\|_{L^p(\bar{\Omega})}$  at the end of the injection, i.e.,  $t = 5$  s.

We need to specify the norm  $\|\cdot\|_{L^p(\bar{\Omega})}$  and the domain  $\bar{\Omega}$  before studying Assumption 2.1. Because we use the Galerkin method and choose to work in the Hilbert space as in Eq. (38), it is natural to use  $L^2(\Omega_0)$ . However as discussed in Section 5.1, the geometry  $\Omega_0$  of the tissue is chosen large enough so as to eliminate the boundary effect, thus the measure of  $\Omega_0$  should be eliminated. We use, instead, the following two space norms:  $L^2(\Omega_e^B)$  and  $L^\infty(\Omega_0)$ . The Jacobian determinant and its approximation error are listed in Table 1, for  $E = 10, 50, 100$  kPa, and  $k_0 = 0.1, 1, 10$  D. The results using the two space norms are consistent. In the rest of the paper, we use  $\|\cdot\|_{L^\infty(\Omega_0)}$  and denote it as  $\|\cdot\|_{L^\infty}$ .

Table 1 indicates that when  $k_0$  is large (10 D),  $\|J_s - \tilde{J}_s\|_{L^\infty}$  is negligible for all values of Young’s modulus studied (10, 50, 100 kPa), but  $\|J_s\|_{L^\infty}$  is small only for  $E = 50$  and 100 kPa. Thus, Assumption 2.1 is satisfied except for  $E = 10$  kPa, even though in this case  $\|J_s - \tilde{J}_s\|_{L^\infty}$  is trivial,  $\|J_s\|_{L^\infty}$  is still too large. When  $k_0$  is of an intermediate value (1 D),  $\|J_s - \tilde{J}_s\|_{L^\infty}$  is small for  $E = 100$  kPa but large for  $E = 10$  kPa. The Jacobian determinant ( $\|J_s\|_{L^\infty}$ ) is large for all  $E$  studied, and Assumption 2.1 is not fulfilled. When  $k_0$  is small (0.1 D), both the Jacobian determinant and its approximation error are large for the range of  $E$  studied, therefore the infinitesimal deformation assumption is violated.

This section serves as the first step of modeling subcutaneous injection using linear poro-elasticity. It is necessary to check if the infinitesimal deformation Assumption 2.1 is satisfied for different tissue properties such as  $E, k_0$ , which should be obtained from experiments.

**Table 1**

The Jacobian determinant ( $\|J_s\|_{L^p(\overline{\Omega})}$ ) and its approximation error ( $\|J_s - \tilde{J}_s\|_{L^p(\overline{\Omega})}$ ), in the bracket) at the end of the injection ( $t = 5$  s) with  $\nu = 0.49$ . The coarse mesh, Fig. 7, is used, and  $V_h^1 \times Q_h$  are the trial and test function spaces.

	$E = 10$ kPa	$E = 50$ kPa	$E = 100$ kPa
$\ \cdot\ _{L^p(\overline{\Omega})} = \ \cdot\ _{L^2(\Omega_0^{\beta})}$			
$k_0 = 10$ D	1.12 ( $4.78 \times 10^{-3}$ )	1.02 ( $1.89 \times 10^{-4}$ )	1.01 ( $4.73 \times 10^{-5}$ )
$k_0 = 1$ D	2.71 (0.53)	1.26 ( $1.94 \times 10^{-2}$ )	1.12 ( $4.78 \times 10^{-3}$ )
$k_0 = 0.1$ D	117.29 (104.63)	5.71 (2.35)	2.71 (0.53)
$\ \cdot\ _{L^p(\overline{\Omega})} = \ \cdot\ _{L^\infty(\Omega_0)}$			
$k_0 = 10$ D	1.15 ( $6.65 \times 10^{-3}$ )	1.03 ( $2.63 \times 10^{-4}$ )	1.01 ( $6.56 \times 10^{-5}$ )
$k_0 = 1$ D	3.16 (0.75)	1.31 ( $2.70 \times 10^{-2}$ )	1.15 ( $6.65 \times 10^{-3}$ )
$k_0 = 0.1$ D	174.09 (159.13)	7.19 (3.37)	3.16 (0.75)

**Remark 5.2.** To justify the choices of the mesh, time step, injection rate and single-layer simplification of the tissue, additional results are presented in Appendix.

### 5.3. Comparison of the linear and nonlinear poro-elastic models

From the previous section, we know that the infinitesimal deformation assumption of the linear poro-elastic model is violated for  $k_0 = 1$  D. The nonlinear model presented in Eq. (36) is not subjected to such limitation. In this section, we use both the linear and nonlinear models to study subcutaneous injection and compare the simulation results.

The model parameters of the Ogden hyperelastic model [26] are shown in Eq. (51). Additionally, we assume  $\phi_0 = 0.1$  and  $\nu = 0.49$ , such that Young’s modulus ( $E = 13.75$  kPa) used in the linear model can be obtained from Eq. (26) and  $\mu = E/(2(1 + \nu))$ . The coarse mesh shown in Fig. 7 is used, and the trial and test function spaces are taken to be  $V_h^1 \times Q_h$ . The injection process is as described in Fig. 5 and the time step is  $\Delta t = 0.01$  s. Eq. (47) is used as the stopping criterion of the fixed-stress iterative scheme, and the tolerance is chosen as  $TOL_{FS} = 5.0 \times 10^{-6}$ .

Two initial permeability values are studied, namely,  $k_0 = 1$  and 10 D. Further reducing the permeability leads to negative Jacobian which violates the constitutive relation of the solid. We present pressure at the injection site **B** and the observation site **C**, the vertical displacement at the skin surface **A**, and the Jacobian determinant ( $\|J_s\|_{L^\infty}$ ) obtained from linear and nonlinear models for  $k_0 = 10$  D in Fig. 8 and 1 D in Fig. 9.

As shown in Fig. 8, when  $k_0 = 10$  D, the pressure profile at the injection site **B** (Fig. 8(a)) of the nonlinear model differs slightly from that of the linear model. Pressure profiles at the observation site **C** (Fig. 8(b)) are similar for both linear and nonlinear models, and so are the vertical displacement profiles at the skin surface **A** (Fig. 8(c)). The declining rates of the pressure at **C** and of the vertical displacement at **A** after injection ( $t > 5$  s) are slightly slower for the nonlinear model. The Jacobian determinant (Fig. 8(d)) of the linear model is slightly greater than that of the nonlinear model. We conclude that for  $k_0 = 10$  D, the tissue deformation is only large at the injection site **B** but is small further away, such that the linear model is a good approximation of the nonlinear model everywhere except at the injection site.

When  $k_0 = 1$  D, Fig. 9(a) shows that the linear model overpredicts the pressure at the injection site (**B**) by 1300%; away from the injection site, the pressure profile at **C** (Fig. 9(b)) is slightly higher for the linear model, and this is also true for the vertical displacement at **A** (Fig. 9(c));  $\|J_s\|_{L^\infty}$  of the linear model is significantly larger than that of the nonlinear model, see Fig. 9(d). To summarize, for small permeability ( $k_0 = 1$  D), the tissue is under large deformation not only at the injection site but also away from it. The infinitesimal deformation Assumption 2.1 of the linear model is not satisfied and we need to resort to the nonlinear model to capture such large deformation.

## 6. Conclusion

In this work, we have used poro-elasticity to model subcutaneous injection of mAbs. The first contribution of this work is the fixed-stress split of the nonlinear poro-elastic model. Convergence studies under spatial and temporal

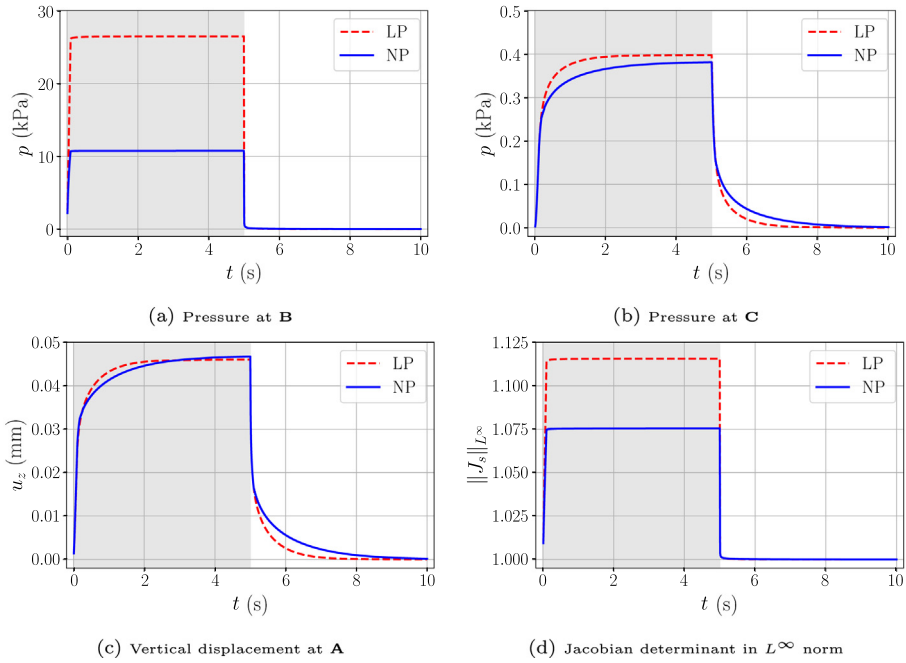


**Fig. 8.** Comparison of pressure, displacement, and the Jacobian determinant for linear and nonlinear poro-elastic models with  $k_0 = 10$  D,  $\nu = 0.49$ , and  $\phi_{f,0} = 0.1$ . The shaded area represents the injection process. Abbreviation: LP, linear model; NP, nonlinear model.

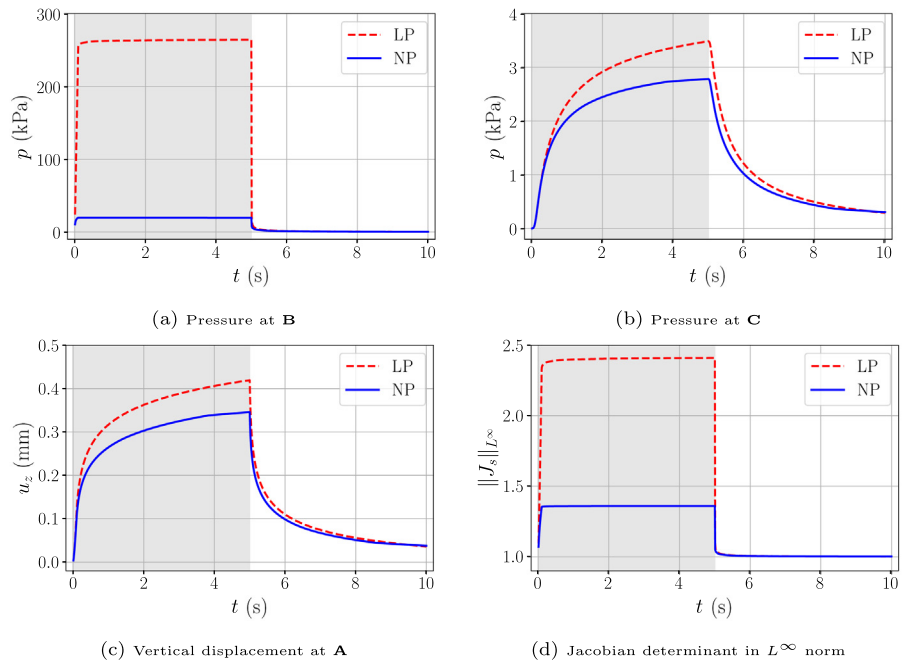


**Fig. 9.** Comparison of pressure, displacement, and the Jacobian determinant for linear and nonlinear poro-elastic models with  $k_0 = 1$  D,  $\nu = 0.49$ , and  $\phi_{f,0} = 0.1$ . The shaded area represents the injection process. Abbreviation: LP, linear model; NP, nonlinear model.

refinements are performed and optimal convergence rates are recovered using a fine solution as the reference solution. The fixed-stress split enables us to decouple the system into two equations, i.e., conservation of mass

and momentum, and to solve the nonlinear coupled system in an iterative procedure, which is more robust than the monolithic scheme. This fixed-stress split iterative scheme can be extended to other poro-elastic models by identifying the volumetric mean stress and assuming it to be constant between two iterations.

Another contribution is that we proposed to validate the infinitesimal deformation assumption of the linear model before applying it to study subcutaneous injection. By evaluating the Jacobian determinant and its approximation error, we have shown that for an average injection rate of about 0.4 mL/s (2 mL over 5 s), whether linear poro-elasticity is valid in the context of subcutaneous injection depends on the material properties of the tissue, such as Young's modulus and initial permeability. The reported values of the Yong's modulus and permeability in the literature cover a wide range. We found that the infinitesimal deformation assumption is fulfilled only for a small range of material properties studied ( $E = 50$ , and  $100$  kPa,  $\nu = 0.49$ , and  $k_0 = 10$  D). For the rest of the cases, especially  $k_0 = 0.1$ , and  $1$  D, the solid deformation becomes so large that the linear model is not valid.

Then, we adopted a nonlinear kinematic poro-elastic model, used in [10,17,37], combined with the Ogden hyperelastic constitutive relation of the solid to study subcutaneous injection. Using model parameters ( $E = 13.75$  kPa,  $\nu = 0.49$ ) taken from experiments of the human adipose tissue [26], we compared numerical solutions of the linear and nonlinear poro-elastic models. We observed that for large permeability ( $k_0 = 10$  D), the deformation is large only near the injection site. The numerical solutions of the linear and nonlinear models differ at the injection site but are in good agreement further away. For small permeability ( $k_0 = 1$  D), the linear model overpredicts the pressure and the deformation not only near the injection site but also away from it.

This is the second work of modeling subcutaneous injection using poro-elasticity and many challenging issues remain to be addressed. In this work, we have chosen the initial permeability ( $k_0$ ) to be greater than 1 D for the nonlinear model. For the injection model shown in Fig. 6, further reducing the permeability results in negative Jacobian determinant which violates the solid constitutive relation in the nonlinear model. Therefore, it is worthwhile to adopt other injection models, such as, smooth volumetric injection rate over time or modeling the injection as a flux boundary condition, so that a smaller permeability ( $k_0$ ) can be used. Viscous behavior has been observed in adipose tissue in [22,24,25,27,64]. Then, it is interesting to use poro-viscoelastic models to study subcutaneous injection. Besides, the computational cost is another challenging topic for nonlinear poro-elastic models. Large deformation only takes place near the injection site and the infinitesimal deformation assumption is still valid further away from the injection site. It will save computational cost if domain decomposition [65] is used to couple the linear and nonlinear poro-elastic models.

### Declaration of competing interest

The authors declare that they have no known competing financial interests or personal relationships that could have appeared to influence the work reported in this paper.

### Acknowledgments

This work is partially supported by Eli Lilly and company, United States. We greatly appreciate the comments from the reviewers which lead to significant improvement of the paper.

### Appendix

We present additional results using different meshes, time steps, and injection rates. A three-layer tissue model is also studied in this section. It is worth mentioning that the linear poro-elastic model, Eq. (35), is used, and the model parameters are the same as those in Fig. 9 other than specified.

#### A.1. Mesh study

In this section, we use a fine mesh near the injection site to study the subcutaneous injection. The motivation is to compare the numerical solution with that of the coarse mesh shown in Fig. 7. The refinement region near the injection site of the fine mesh is shown in Fig. A.10. A total of six-levels of refinement is carried out so that the smallest mesh size is still 0.15625 mm.

First of all, we use the two meshes (Figs. 7 and A.10) combined with first- and second-order elements for the displacement to study the numerical validation of the linear model for different permeability and Young's modulus

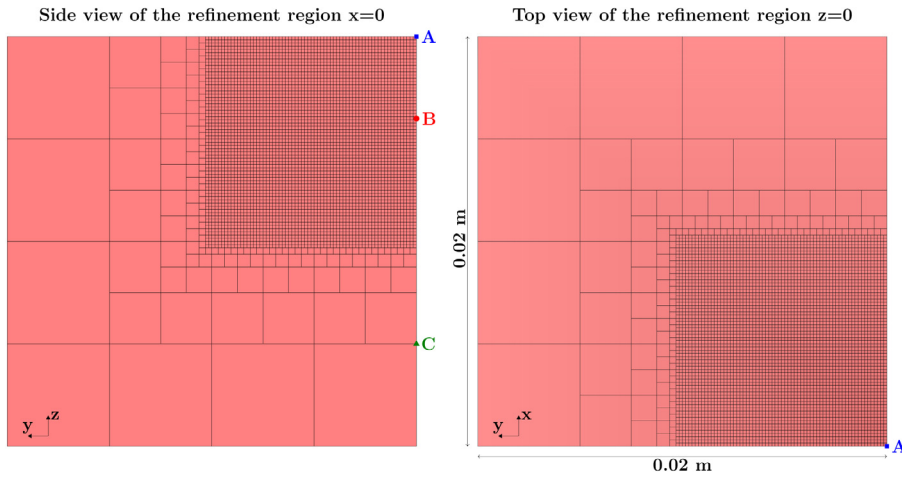


Fig. A.10. Side and top views of the fine mesh at the refinement region in Fig. 5.

Table A.2

The Jacobian determinant ( $\|J_s\|_{L^\infty}$ ) and its approximation error ( $\|J_s - \tilde{J}_s\|_{L^\infty}$ , in the bracket) at the end of the injection ( $t = 5$  s) with  $\nu = 0.49$ , using different meshes (the coarse and fine meshes are referred as in Figs. 7 and A.10 respectively), and trial and test functions.

	$E = 10$ kPa	$E = 50$ kPa	$E = 100$ kPa
Fine mesh and $V_h^1 \times Q_h$			
$k_0 = 10$ D	1.15 ( $6.81 \times 10^{-3}$ )	1.03 ( $2.69 \times 10^{-4}$ )	1.01 ( $6.72 \times 10^{-5}$ )
$k_0 = 1$ D	3.19 (0.77)	1.31 ( $2.70 \times 10^{-2}$ )	1.15 ( $6.65 \times 10^{-3}$ )
$k_0 = 0.1$ D	174.09 (159.13)	7.19 (3.37)	3.19 (0.77)
Coarse mesh and $V_h^2 \times Q_h$			
$k_0 = 10$ D	1.16 ( $7.96 \times 10^{-3}$ )	1.03 ( $3.14 \times 10^{-4}$ )	1.02 ( $7.84 \times 10^{-5}$ )
$k_0 = 1$ D	3.44 (0.91)	1.34 ( $3.24 \times 10^{-2}$ )	1.16 ( $7.96 \times 10^{-3}$ )
$k_0 = 0.1$ D	220.68 (204.55)	8.20 (4.15)	3.44 (0.91)
Fine mesh and $V_h^2 \times Q_h$			
$k_0 = 10$ D	1.16 ( $8.02 \times 10^{-3}$ )	1.03 ( $3.17 \times 10^{-4}$ )	1.02 ( $7.90 \times 10^{-5}$ )
$k_0 = 1$ D	3.45 (0.92)	1.34 ( $3.26 \times 10^{-2}$ )	1.16 ( $8.02 \times 10^{-3}$ )
$k_0 = 0.1$ D	222.89 (206.71)	8.25 (4.19)	3.45 (0.92)

values. The model parameters are the same as those in Section 5.2. The Jacobian determinant and its approximation error are presented in Table A.2. From Tables 1 and A.2, we observe that the Jacobian determinant obtained using the two meshes, and linear and quadratic elements are similar.

In addition, we also compare the pressure, displacement and the Jacobian determinant of the linear model at the observation points using the coarse and fine meshes. The model parameters are those used in Fig. 9. As shown in Fig. A.11, the simulation results at the observation sites are similar using the two meshes. Therefore, we conclude that the coarse mesh is enough to obtain accurate results.

### A.2. Time step

In this section, we justify the choice of the time step. The simulation of the linear model in Fig. 9 is run using a smaller time step  $\Delta t = 0.001$  s. The simulation results using the two time steps (0.01 and 0.001 s) are almost identical as shown in Fig. A.12. Thus, we have justified the use of the time step  $\Delta t = 0.01$  s.

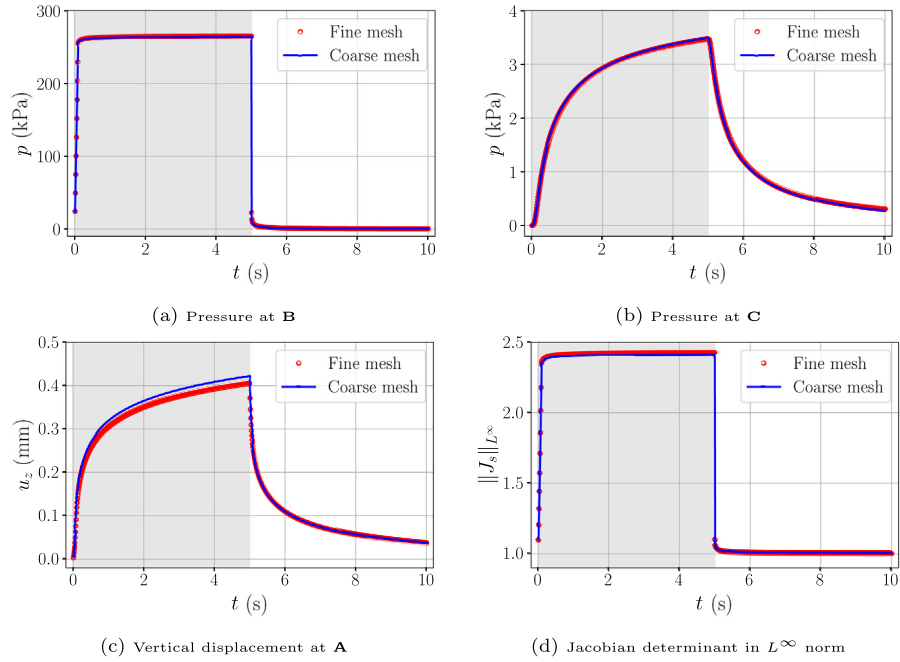


**Fig. A.11.** Comparison of the pressure, displacement, and the Jacobian determinant of the linear model using the coarse (Fig. 7) and fine (Fig. A.10) meshes. The material parameters are as follows  $k_0 = 1$  D,  $\nu = 0.49$ ,  $E = 13.75$  kPa,  $\phi_{f,0} = 0.1$ . The time step is  $\Delta t = 0.01$  s. The shaded area represents the injection process.

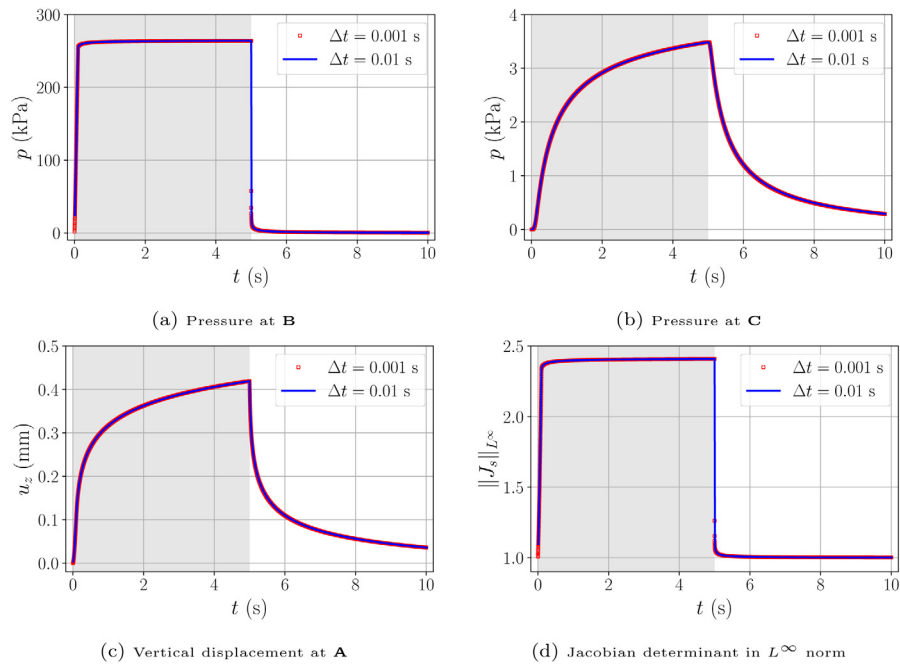


**Fig. A.12.** Comparison of the pressure, displacement, and the Jacobian determinant of the linear model using  $\Delta t = 0.01$  and  $0.001$  s. The material parameters are as follows  $k_0 = 1$  D,  $\nu = 0.49$ ,  $E = 13.75$  kPa,  $\phi_{f,0} = 0.1$ . The coarse mesh (Fig. 7) is used. The shaded area represents the injection process.

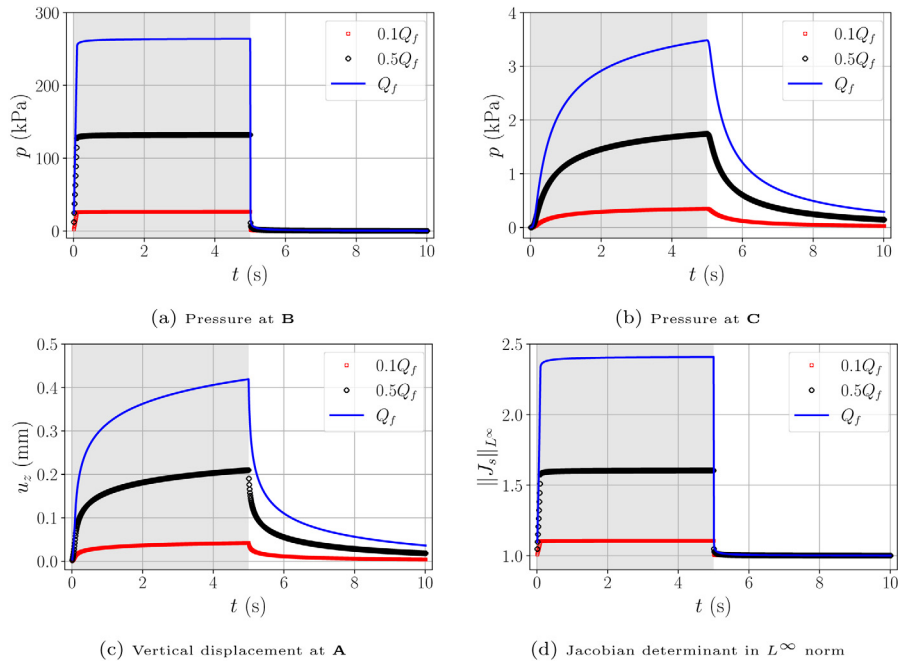


**Fig. A.13.** Comparison of the pressure, displacement, and the Jacobian determinant of the linear model using different injection rates. The material parameters are as follows  $k_0 = 1$  D,  $\nu = 0.49$ ,  $E = 13.75$  kPa,  $\phi_{f,0} = 0.1$ . The coarse mesh (Fig. 7) is used, and the time step is  $\Delta t = 0.01$  s. The shaded area represents the injection process.

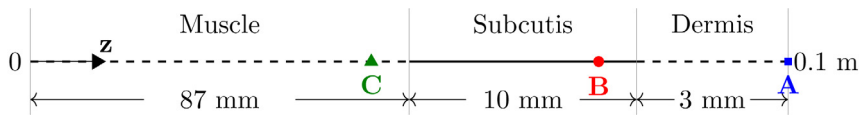


**Fig. A.14.** Three-layer skin model. The schematic thickness of each layer is exaggerated and does not represent the values denoted. The Young’s modulus of the muscle, subcutis and dermis layers is taken to be 50 kPa [66], 13.75 kPa [26] and 100 kPa [67,68], respectively.

**A.3. Injection rate**

As discussed in Remark 5.1, the injection rate plays the vital role in the study of subcutaneous injection. Simulation results with smaller injection rates ( $0.5Q_f$  and  $0.1Q_f$ ) of those in Fig. 9 for the linear model are shown in Fig. 5. It is evident that higher injection rates lead to larger deformation and pore pressure (see Fig. A.13).

**A.4. Three-layer skin**

In Section 5, we have modeled the skin as a homogeneous single-layer tissue. However, as shown in Fig. 5, the skin consists of multi-layers including, epidermis, dermis, subcutis, and muscle. In this section, we divide the cube in Fig. 5 into three layers along the vertical ( $z$ ) direction as in Fig. A.14. The thickness of each layer is referenced from [69]. The Young’s modulus of the muscle, subcutis and dermis layers is taken to be 50 kPa [66], 13.75 kPa [26] and 100 kPa [67,68], respectively. The rest of the model parameters are assumed to be identical for all three layers, and they are the same as in Fig. 9.

The simulation results are compared using a three-layer skin model against the single-layer model. As depicted in Fig. A.15, the pressure at the injection site (Fig. A.15(a)) and the maximum Jacobian are the same for the three-layer and single-layer models. This is because the injection happens in the subcutaneous layer, and the large deformation occurs at the injection site. As shown in Fig. A.14, the Young’s modulus at A and C is different from that of the single-layer model. Thus, the vertical displacement in Fig. A.15(c) and pore pressure in Fig. A.15(b) are different

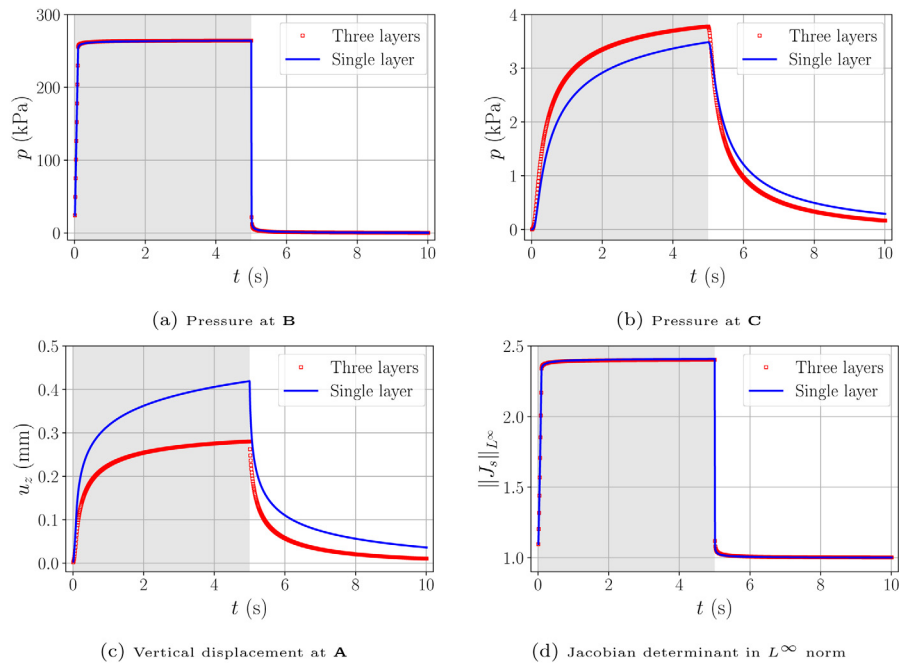


**Fig. A.15.** Comparison of the pressure, displacement, and the Jacobian determinant of the linear model using the single-layer and three-layer tissue models. The material parameters are as follows  $k_0 = 1$  D,  $\nu = 0.49$ ,  $\phi_{f,0} = 0.1$ . The coarse mesh (Fig. 7) is used, and the time step is  $\Delta t = 0.01$  s. The shaded area represents the injection process.

as expected. The three-layer model confirms that the infinitesimal deformation [Assumption 2.1](#) of the linear model is violated and that the nonlinear poro-elastic model is necessary to study subcutaneous injection.

## References

- [1] D.S. Dimitrov, Therapeutic proteins, in: *Therapeutic Proteins*, Springer, 2012, pp. 1–26.
- [2] M.F. Haller, Converting intravenous dosing to subcutaneous dosing with recombinant human hyaluronidase, *Pharm. Tech.* 31 (2007) 861–864.
- [3] C. Jackisch, V. Müller, C. Maintz, S. Hell, B. Ataseven, Subcutaneous administration of monoclonal antibodies in oncology, *Geburtshilfe Frauenheilkunde* 74 (4) (2014) 343.
- [4] C. Porter, G. Edwards, S.A. Charman, Lymphatic transport of proteins after sc injection: implications of animal model selection, *Adv. Drug Deliv. Rev.* 50 (1–2) (2001) 157–171.
- [5] O. Shpilberg, C. Jackisch, Subcutaneous administration of rituximab (MabThera) and trastuzumab (Herceptin) using hyaluronidase, *Br. J. Cancer* 109 (6) (2013) 1556–1561.
- [6] K. Comley, N. Fleck, Deep penetration and liquid injection into adipose tissue, *J. Mech. Mater. Struct.* 6 (1) (2011) 127–140.
- [7] D. Kang, D. Oh, G. Fu, J. Anderson, M. Zepeda, Porcine model to evaluate local tissue tolerability associated with subcutaneous delivery of protein, *J. Pharmacol. Toxicol. Methods* 67 (3) (2013) 140–147.
- [8] A. Malandrino, E. Moendarbary, Poroelasticity of living tissues, in: *Encyclopedia of Biomedical Engineering*, Vol. 2, Elsevier, 2019, pp. 238–245.
- [9] B.R. Simon, Multiphase poroelastic finite element models for soft tissue structures, *Appl. Mech. Rev.* 45 (6) (1992) 191–218.
- [10] E. Comellas, S. Budday, J.-P. Pelteret, G.A. Holzapfel, P. Steinmann, Modeling the porous and viscous responses of human brain tissue behavior, *Comput. Methods Appl. Mech. Engrg.* 369 (2020) 113128.
- [11] W. Ehlers, A. Wagner, Constitutive and computational aspects in tumor therapies of multiphase brain tissue, in: *Computer Models in Biomechanics*, Springer, 2013, pp. 263–276.
- [12] W. Ehlers, A. Wagner, Multi-component modelling of human brain tissue: a contribution to the constitutive and computational description of deformation, flow and diffusion processes with application to the invasive drug-delivery problem, *Comput. Methods Biomech. Biomed. Eng.* 18 (8) (2015) 861–879.
- [13] R. de Rooij, E. Kuhl, Constitutive modeling of brain tissue: current perspectives, *Appl. Mech. Rev.* 68 (1) (2016).
- [14] M. de Lucio, M. Bures, A.M. Ardekani, P.P. Vlachos, H. Gomez, Isogeometric analysis of subcutaneous injection of monoclonal antibodies, *Comput. Methods Appl. Mech. Eng.*, 373, 113550.

- [15] W. Ehlers, N. Karajan, B. Markert, An extended biphasic model for charged hydrated tissues with application to the intervertebral disc, *Biomech. Model. Mechanobiol.* 8 (3) (2009) 233.
- [16] G.A. Holzapfel, R.W. Ogden, *Biomechanics: Trends in Modeling and Simulation*, Vol. 316, Springer, 2017.
- [17] W. Ehlers, *Porous Media: Theory, Experiments and Numerical Applications*, Springer Science & Business Media, 2002.
- [18] S. Hirsch, A biphasic poroelasticity model for soft tissue, in: *Quantification of Biophysical Parameters in Medical Imaging*, Springer, 2018, pp. 71–88.
- [19] M.A. Biot, General theory of three-dimensional consolidation, *J. Appl. Phys.* 12 (2) (1941) 155–164.
- [20] M.A. Biot, Theory of propagation of elastic waves in a fluid-saturated porous solid. II. Higher frequency range, *J. Acoust. Soc. Am.* 28 (2) (1956) 179–191.
- [21] M.A. Biot, G. Temple, Theory of finite deformations of porous solids, *Indiana Univ. Math. J.* 21 (7) (1972) 597–620.
- [22] J.L. Calvo-Gallego, J. Domínguez, T.G. Cía, G.G. Ciriza, J. Martínez-Reina, Comparison of different constitutive models to characterize the viscoelastic properties of human abdominal adipose tissue. A pilot study, *J. Mech. Behav. Biomed. Mater.* 80 (2018) 293–302.
- [23] K. Comley, N. Fleck, The compressive response of porcine adipose tissue from low to high strain rate, *Int. J. Impact Eng.* 46 (2012) 1–10.
- [24] P.N. Patel, C.K. Smith, C.W. Patrick Jr, Rheological and recovery properties of poly (ethylene glycol) diacrylate hydrogels and human adipose tissue, *J. Biomed. Mater. Res. A* 73 (3) (2005) 313–319.
- [25] A.M. Sims, T. Stait-Gardner, L. Fong, J.W. Morley, W.S. Price, M. Hoffman, A. Simmons, K. Schindhelm, Elastic and viscoelastic properties of porcine subdermal fat using MRI and inverse FEA, *Biomech. Model. Mechanobiol.* 9 (6) (2010) 703–711.
- [26] Z. Sun, S.-H. Lee, B.D. Gepner, J. Rigby, J.J. Hallman, J.R. Kerrigan, Comparison of porcine and human adipose tissue loading responses under dynamic compression and shear: A pilot study, *J. Mech. Behav. Biomed. Mater.* 113 (2021) 104112.
- [27] G. Sommer, M. Eder, L. Kovacs, H. Pathak, L. Bonitz, C. Mueller, P. Regitnig, G.A. Holzapfel, Multiaxial mechanical properties and constitutive modeling of human adipose tissue: a basis for preoperative simulations in plastic and reconstructive surgery, *Acta Biomater.* 9 (11) (2013) 9036–9048.
- [28] J. Kim, H.A. Tchelepi, R. Juanes, Stability and convergence of sequential methods for coupled flow and geomechanics: Fixed-stress and fixed-strain splits, *Comput. Methods Appl. Mech. Engrg.* 200 (13–16) (2011) 1591–1606.
- [29] J. Kim, H.A. Tchelepi, R. Juanes, et al., Stability, accuracy and efficiency of sequential methods for coupled flow and geomechanics, in: *SPE Reservoir Simulation Symposium*, Society of Petroleum Engineers, 2009.
- [30] A. Mikelić, B. Wang, M.F. Wheeler, Numerical convergence study of iterative coupling for coupled flow and geomechanics, *Comput. Geosci.* 18 (3–4) (2014) 325–341.
- [31] A. Mikelić, M.F. Wheeler, Convergence of iterative coupling for coupled flow and geomechanics, *Comput. Geosci.* 17 (3) (2013) 455–461.
- [32] F. Irzal, J.J. Remmers, C.V. Verhoosel, R. de Borst, Isogeometric finite element analysis of poroelasticity, *Int. J. Numer. Anal. Methods Geomech.* 37 (12) (2013) 1891–1907.
- [33] M. Rahrah, F. Vermolen, A moving finite element framework for fast infiltration in nonlinear poroelastic media, *Comput. Geosci.: Model. Simul. Data Anal.* (2020).
- [34] M.A.B. Reverón, K. Kumar, J.M. Nordbotten, F.A. Radu, Iterative solvers for Biot model under small and large deformations, *Comput. Geosci.* (2020) 1–13.
- [35] L.C. Auton, C.W. MacMinn, From arteries to boreholes: transient response of a poroelastic cylinder to fluid injection, *Proc. R. Soc. A* 474 (2216) (2018) 20180284.
- [36] T. Bertrand, J. Peixinho, S. Mukhopadhyay, C.W. MacMinn, Dynamics of swelling and drying in a spherical gel, *Phys. Rev. A* 6 (6) (2016) 064010.
- [37] C.W. MacMinn, E.R. Dufresne, J.S. Wettlaufer, Large deformations of a soft porous material, *Phys. Rev. A* 5 (4) (2016) 044020.
- [38] W. Ehlers, G. Eipper, Finite elastic deformations in liquid-saturated and empty porous solids, in: *Porous Media: Theory and Experiments*, Springer, 1999, pp. 179–191.
- [39] O. Coussy, *Poromechanics*, John Wiley & Sons, 2004.
- [40] J.E. Marsden, T.J. Hughes, *Mathematical Foundations of Elasticity*, Courier Corporation, 1994.
- [41] C.J. van Duijn, A. Mikelić, T. Wick, A monolithic phase-field model of a fluid-driven fracture in a nonlinear poroelastic medium, *Math. Mech. Solids* 24 (5) (2019) 1530–1555.
- [42] C. Van Duijn, A. Mikelić, *Mathematical theory of nonlinear single-phase poroelasticity*, 2019, Preprint hal-02144933, Lyon June.
- [43] S. Budday, G. Sommer, C. Birkl, C. Langkammer, J. Haybaeck, J. Kohert, M. Bauer, F. Paulsen, P. Steinmann, E. Kuhl, et al., Mechanical characterization of human brain tissue, *Acta Biomater.* 48 (2017) 319–340.
- [44] R.W. Ogden, Large deformation isotropic elasticity—on the correlation of theory and experiment for incompressible rubberlike solids, *Proc. R. Soc. Lond. Ser. A Math. Phys. Eng. Sci.* 326 (1567) (1972) 565–584.
- [45] D. Arndt, W. Bangerth, B. Blais, T.C. Clevenger, M. Fehling, A.V. Grayver, T. Heister, L. Heltai, M. Kronbichler, M. Maier, P. Munch, J.-P. Pelteret, R. Rastak, I. Thomas, B. Turcksin, Z. Wang, D. Wells, The deal.II library, version 9.2, *J. Numer. Math.* 28 (3) (2020) 131–146, <http://dx.doi.org/10.1515/jnma-2020-0043>, URL <https://dealii.org/deal92-preprint.pdf>.
- [46] W. Bangerth, R. Hartmann, G. Kanschat, deal.II – a General purpose object oriented finite element library, *ACM Trans. Math. Software* 33 (4) (2007) 24/1–24/27.
- [47] M. Bause, F.A. Radu, U. Köcher, Space–time finite element approximation of the Biot poroelasticity system with iterative coupling, *Comput. Methods Appl. Mech. Engrg.* 320 (2017) 745–768.
- [48] I. Shovkun, D.N. Espinoza, Fracture propagation in heterogeneous porous media: pore-scale implications of mineral dissolution, *Rock Mech. Rock Eng.* 52 (9) (2019) 3197–3211.

- [49] I. Shovkun, D.N. Espinoza, Propagation of toughness-dominated fluid-driven fractures in reactive porous media, *Int. J. Rock Mech. Min. Sci.* 118 (2019) 42–51.
- [50] M.F. Wheeler, T. Wick, S. Lee, IPACS: Integrated phase-field advanced crack propagation simulator. An adaptive, parallel, physics-based-discretization phase-field framework for fracture propagation in porous media, *Comput. Methods Appl. Mech. Engrg.* 367 (2020) 113124.
- [51] X. Lu, M.F. Wheeler, Three-way coupling of multiphase flow and poromechanics in porous media, *J. Comput. Phys.* 401 (2020) 109053.
- [52] S. Lee, M.F. Wheeler, T. Wick, Iterative coupling of flow, geomechanics and adaptive phase-field fracture including level-set crack width approaches, *J. Comput. Appl. Math.* 314 (2017) 40–60.
- [53] A. Mikelić, M. Wheeler, T. Wick, Phase-field modeling through iterative splitting of hydraulic fractures in a poroelastic medium, *GEM-Int. J. Geomath.* 10 (1) (2019) 2.
- [54] S. Lee, M.F. Wheeler, T. Wick, Pressure and fluid-driven fracture propagation in porous media using an adaptive finite element phase field model, *Comput. Methods Appl. Mech. Engrg.* 305 (2016) 111–132.
- [55] T. Sacado Project Team, The sacado project website, 2020, URL <https://trilinos.github.io/sacado.html>,
- [56] A.V. Badkar, R.B. Gandhi, S.P. Davis, M.J. LaBarre, Subcutaneous delivery of high-dose/volume biologics: Current status and prospect for future advancements, *Drug Des. Dev. Therapy* 15 (2021) 159.
- [57] B. Bittner, W. Richter, J. Schmidt, Subcutaneous administration of biotherapeutics: an overview of current challenges and opportunities, *BioDrugs* 32 (5) (2018) 425–440.
- [58] R. Mathaes, A. Koulov, S. Joerg, H.-C. Mahler, Subcutaneous injection volume of biopharmaceuticals—pushing the boundaries, *J. Pharm. Sci.* 105 (8) (2016) 2255–2259.
- [59] I. Usach, R. Martinez, T. Festini, J.-E. Peris, Subcutaneous injection of drugs: literature review of factors influencing pain sensation at the injection site, *Adv. Ther.* 36 (11) (2019) 2986–2996.
- [60] A.C. Guyton, K. Scheel, D. Murphree, Interstitial fluid pressure: III. Its effect on resistance to tissue fluid mobility, *Circ. Res.* 19 (2) (1966) 412–419.
- [61] H. Kim, H. Park, S.J. Lee, Effective method for drug injection into subcutaneous tissue, *Sci. Rep.* 7 (1) (2017) 1–11.
- [62] N.P. Reddy, G.V.B. Cochran, T.A. Krouskop, Interstitial fluid flow as a factor in decubitus ulcer formation, *J. Biomech.* 14 (12) (1981) 879–881.
- [63] M. Thomsen, A. Hernandez-Garcia, J. Mathiesen, M. Poulsen, D.N. Sørensen, L. Tarnow, R. Feidenhans, Model study of the pressure build-up during subcutaneous injection, *PLoS One* 9 (8) (2014) e104054.
- [64] M. Geerligs, G.W. Peters, P.A. Ackermans, C.W. Oomens, F. Baaijens, Linear viscoelastic behavior of subcutaneous adipose tissue, *Biorheology* 45 (6) (2008) 677–688.
- [65] V. Girault, M.F. Wheeler, T. Almani, S. Dana, A priori error estimates for a discretized poro-elastic–elastic system solved by a fixed-stress algorithm, *Oil Gas Sci. Technol.–Rev. IFP Energies nouvelles* 74 (2019) 24.
- [66] B.C.W. Kot, Z.J. Zhang, A.W.C. Lee, V.Y.F. Leung, S.N. Fu, Elastic modulus of muscle and tendon with shear wave ultrasound elastography: variations with different technical settings, *PLoS One* 7 (8) (2012) e44348.
- [67] P.G. Agache, C. Monneur, J.L. Leveque, J. De Rigal, Mechanical properties and Young’s modulus of human skin in vivo, *Arch. Dermatol. Res.* 269 (3) (1980) 221–232.
- [68] C. Paillet-Mattei, S. Bec, H. Zahouani, In vivo measurements of the elastic mechanical properties of human skin by indentation tests, *Med. Eng. Phys.* 30 (5) (2008) 599–606.
- [69] S. Muraki, K. Fukumoto, O. Fukuda, Prediction of the muscle strength by the muscle thickness and hardness using ultrasound muscle hardness meter, *Springerplus* 2 (1) (2013) 1–7.